Relationship between Three-dimensional Crack Morphology and Macroscopic Mechanical Properties of Hydrogen-related Fracture in Martensitic Steel

Akinobu Shibata, Yazid Madi, Jacques Besson, Akiko Nakamura, Taku Moronaga, Kazuho Okada, Ivan Gutierrez-Urrutia, Toru Hara

Special Issue on “New Developments in Elucidation of Hydrogen Embrittlement Phenomena from the Incubation Stage to Fracture”

Relationship between three-dimensional crack morphology and macroscopic mechanical properties of hydrogen-related fracture in martensitic steel

Akinobu Shibata*, Yazid Madi, Jacques Besson, Akiko Nakamura, Taku Moronaga, Kazuho Okada, Ivan Gutierrez-Urrutia and Toru Hara

* Corresponding author. E-mail: SHIBATA.Akinobu@nims.go.jp

Received date: August 6, 2023
Accepted date: November 2, 2023
Advance published date: November 11, 2023

DOI: https://doi.org/10.2355/isijinternational.ISIJINT-2023-316

Please cite this article as:

A. Shibata, Y. Madi, J. Besson, A. Nakamura, T. Moronaga, K. Okada, I. Gutierrez-Urrutia and T. Hara: *ISIJ Int.*, (2023), https://doi.org/10.2355/isijinternational.ISIJINT-2023-316

Relationship between three-dimensional crack morphology and macroscopic mechanical properties of hydrogen-related fracture in martensitic steel

Akinobu Shibata [a,*], Yazid Madi [b], Jacques Besson [b], Akiko Nakamura [c], Taku Moronaga [c], Kazuho Okada [a], Ivan Gutierrez-Urrutia [a], Toru Hara [a]

[a] Research Center for Structural Materials, National Institute for Materials Science (NIMS), 1-2-1, Sengen, Tsukuba 305-0047, Japan.

[b] Centre des Matériaux, MINES Paris-PSL, CNRS UMR 7633, BP 87, 91003, Evry, France.

[c] Research Network and Facility Services Division, National Institute for Materials Science (NIMS), 1-2-1, Sengen, Tsukuba 305-0047, Japan.

[*] Corresponding author E-mail: SHIBATA.Akinobu@nims.go.jp

Tel: +81-29-859-2074

Synopsis

In the present study, several parameters related to crack morphology in the case of hydrogen embrittlement were estimated by X-ray computed tomography and correlated with the macroscopic mechanical responses (*J*-integral and tearing modulus) obtained from the fracture mechanics tests. Even when the hydrogen content was high up to 4.00 wt ppm, unstable premature fracture did not immediately occur, and a certain crack-growth resistance could be confirmed. The three-dimensional crack morphology was not continuous with the formation of un-cracked ligaments in the uncharged specimen. In contrast, the hydrogen-related intergranular crack propagated more continuously with a smaller crack opening-displacement. The *J*-integral value monotonically increased with increasing estimated values of the surface area divided by the projected surface area on the macroscopic crack plane, indicating that crack meandering and branching increased the fracture energy. We defined crack-propagated thickness (standard deviation of the crack surface area at each section (parallel to the macroscopic crack plane) divided by the crack surface area) as a parameter representing crack meandering. The tearing modulus increased as the crack-propagated thickness increased, suggesting that crack meandering also increased the crack-growth resistance.

Keywords: hydrogen embrittlement; fracture toughness; crack morphology; three-dimensional analysis; martensitic steel

1. Introduction

Hydrogen embrittlement is a phenomenon that materials exhibit premature brittle fracture due to the presence of hydrogen [1, 2]. Since hydrogen embrittlement is more pronounced in high-strength steels, material design to improve hydrogen embrittlement properties is necessary for the widespread application of advanced high-strength steels. To date, several models for hydrogen-related fracture have been proposed, such as high hydrogen pressure bubbles or voids [3], hydrogen-induced reduction in cohesive energy [4-6], hydrogen-enhanced localized plasticity (so-called HELP) [7-10], and hydrogen-enhanced strain-induced vacancy [11, 12]. The dominant model in actual hydrogen-related fracture depends on several factors, i.e., the strength level of the materials, the constitutive microstructure, the deformation condition, the hydrogen content, and so on. The relationship between the macroscopic mechanical response (degree of hydrogen-induced degradation of macroscopic mechanical properties) and each fracture model remains to be understood.

Typical modes of hydrogen-related fracture in steels are quasi-cleavage and intergranular. According to Hagihara et al. [13], with increasing hydrogen content, the fracture mode changes from quasi-cleavage to intergranular, resulting in more brittle behavior. Martensitic steels are one of the typical high-strength steels. The martensite structure is complicated and consists of several microstructural units with different size scales, such as lath, block, packet, and prior austenite grain [14-17]. The quasi-cleavage fracture corresponds to a transgranular occurring on non-typical cleavage planes (specifically, {011} planes) within the lath, and local plastic deformation plays a crucial role

in the hydrogen-related quasi-cleavage fracture [18-21]. On the other hand, the hydrogen-related intergranular cracks propagate mainly on prior austenite grain boundaries [22-25]. The primitive mechanism of hydrogen-related intergranular cracking is very simple. Segregation of hydrogen reduces the cohesive energy of the boundary, resulting in decohesion of the boundary. The reduction of cohesive energy by hydrogen has been estimated by first-principles calculations [26-29]. Yamaguchi and Kameda [30] performed a combined analysis using first-principles calculations and fracture mechanics tests for intergranular fracture in thermally aged Ni-Cr steels. They reported that the decrease in the boundary cohesive energy is accompanied by a decrease in the plastic work associated with cracking and insisted that the boundary cohesive energy is a very important parameter to account for intergranular cracking.

Previously, we investigated the intergranular fracture behavior of a martensitic steel by multi-scale three-dimensional analysis and found that the intergranular crack propagation along prior austenite grain boundaries is basically irregular and discontinuous with the formation of un-cracked ligaments [31, 32]. The un-cracked ligaments were likely to be formed at the prior austenite grain boundary segments with small misorientation. Because the ductile fracture of the un-cracked ligaments at the later fracture stage would contribute to the macroscopic mechanical responses [33-37], we believe that the crack morphology is also an important parameter affecting the macroscopic fracture toughness. In the present study, the fracture toughness test results previously reported for as-quenched martensitic steel [31, 38] were used to investigate the relationship between three-dimensional

crack morphology and macroscopic mechanical properties of hydrogen-related fracture.

2. Experimental procedure

This study used an Fe-8Ni-0.1C alloy (C: 0.116, Si: 0.005, Mn: 0.01, P: 0.001, S: 0.0015, Al: 0.033, Ni: 7.94, and Fe: balance (mass%)), which is a model steel containing a large amount of nickel to increase the hardenability. The steel plates were austenitized at 1000 °C for 30 min, and then ice-brine quenched and sub-zero cooled in liquid nitrogen to obtain a fully martensitic microstructure. The 0.2% proof strength and tensile strength of the heat-treated specimens evaluated by uniaxial tensile tests were 920 and 1191 MPa, respectively [38]. Pre-cracked compact tension specimens were prepared from the heat-treated plates (width: 25 mm, thickness: 12.5 mm, and net thickness at the root of side grooves: 10 mm). In order to introduce hydrogen, the pre-cracked compact tension specimens were electrochemically charged in an aqueous solution containing 3% NaCl and 3 g L^{-1} NH_4SCN for 3 days at ambient temperature. The current densities employed for hydrogen charging were changed from 0.625 A m^{-2} to 3 A m^{-2}, and the diffusible hydrogen contents (H_D) measured by thermal desorption analysis were 0.28 wt ppm (0.625 A m^{-2}), 0.42 wt ppm (1.25 A m^{-2}), 1.01 wt ppm (2 A m^{-2}), and 4.00 wt ppm (3 A m^{-2}).

The microstructure of the heat-treated specimen was observed by scanning electron microscopy (SEM, JEOL: JSM-7800F and Hitachi High-Tech: SMF-1000) and scanning transmission electron microscopy (STEM, JEOL: JEM-2800 (operated at 200 kV) and JEM-ARM300F (operated at 300

kV)). Thin foils for STEM observation were fabricated using a focused ion beam (FIB) – SEM system (ThermoFisher Scientific: Scios2 and Hitachi High-Tech: SMF-1000). The crack-growth properties were evaluated by unloading compliance tests using the single specimen test method according to ASTM E1820-17 [39]. The unload / reload sequences were performed at a displacement interval of 0.025 mm. The *J*-integral was calculated from $J_{el} + J_{pl}$, where J_{el} was computed from linear elastic fracture mechanics, and J_{pl} was incrementally computed using the plastic area under the load – load-line displacement curve. According to ASTM E1820-17 [39], the crack extension length (Δa) at each stage was evaluated from the elastic compliance obtained by the unload / reload sequences. In order to make the strain rate sufficiently slow, the load-line displacement was set to 2.5×10^{-5} mm s^{-1}, whose initial rate of stress intensity factor for $a_0 / W = 0.5$ was 8.5×10^{-3} MPa $m^{1/2}$ s^{-1}. The details of the mechanical testing are described in the previous paper [38].

The fracture surfaces and cracks in the mid-thickness section after the unloading compliance tests were observed by SEM. X-ray computed tomography (X-ray CT, ZEISS: Xradia 620 Versa) was used to reconstruct the three-dimensional crack morphology. A specimen with dimensions of approximately 2 mm × 16 mm × 1 mm was cut from the mid-thickness region of the tested specimen by spark wire cutting, and absorption contrast images were taken around a 360 ° rotation of the specimen in 0.1 ° steps using an optical magnifying lens (× 4 and × 20 magnification) at an acceleration voltage of 100 kV.

3. Results and Discussion

3.1 Microstructure and mechanical properties

Figure 1 presents (a) SEM image, (b, c) STEM images, and (d) energy dispersive X-ray (EDX) analysis result (sulfur distribution map) of the as heat-treated specimen. The observation areas of (c) and (d) are identical, and the position of prior austenite grain boundary is indicated by the broken line. The specimen exhibits a typical lath martensite structure as shown in **Figure 1** (a, b). The STEM-EDX result indicates that sulfur is segregated at the prior austenite grain boundary (~ 0.12 %), though sulfur was not intentionally added to the steel (the nominal composition of sulfur is 0.0015 %). It has been reported that dissolution of sulfides during austenitization leads to segregation and re-precipitation of sulfur at austenite grain boundaries [40]. The intergranular fracture that occurred even in the uncharged specimen shown below could be attributed to the segregated sulfur at the prior austenite grain boundaries.

Figure 2 (a) presents the $J - \Delta a$ resistance curves of the uncharged specimen and hydrogen-charged specimens with H_D = 0.42 wt ppm and 4.00 wt ppm (the resistance curves of the specimens exactly used for the X-ray CT measurements shown below are indicated by the arrows). All specimens (including the hydrogen-charged specimens) satisfied the required specimen dimensional criteria for obtaining a valid plane-strain J_{IC} according to ASTM E1820-17 [39]. The dimensionless tearing modulus (T_R) obtained from the unloading compliance tests is plotted as a function of H_D in **Figure 2** (b) (the data from our previous paper [38] were reused). The dimensionless tearing modulus is a

parameter representing crack-growth resistance and can be calculated from the following equation;

$$T_R = \frac{E}{\sigma_0^2}\frac{dJ}{d\Delta a} \qquad \text{Eq.1}$$

where E is a Young's modulus (200 GPa), σ_0 is a 0.2 % offset yield strength (920 MPa), and $dJ / d\Delta a$ is an average slope of the linear region in the $J - \Delta a$ resistance curve (after the intersection of the 0.2 mm offset line). For the hydrogen-charged specimens, the J-integral values corresponding to the onset of crack propagation were much lower compared to the uncharged specimen. As shown in **Figure 2** (b), the tearing modulus decreases with increasing H_D. The results indicate that hydrogen promoted crack initiation and decreased crack-growth resistance. However, even when the hydrogen content was high up to 4.00 wt ppm, unstable premature fracture did not immediately occur. We can confirm a certain crack-growth resistance (positive slope of $J - \Delta a$ resistance curve and ~ 0.5 of tearing modulus). It should be noted here that, from a fracture mechanics standpoint, the strict criterion for the initiation of unstable fracture is when the differentiate of crack driving force curve exceeds that of crack-growth resistance curve. Because the present study did not evaluate crack driving force curves, the obtained tearing modulus may not exactly correspond to that assuming stable crack propagation.

3.2 Crack propagation behavior analyzed by SEM and X-ray CT

Figure 3 (a – c) shows the fracture surfaces after the unloading compliance tests in the (a) uncharged specimen, (b) hydrogen-charged specimen with H_D = 0.42 wt ppm, and (c) hydrogen-

charged specimen with H_D = 4.00 wt ppm. The fatigue pre-cracked regions are located on the left side of the figures. All the surfaces mainly consist of intergranular surfaces, although dimples and quasi-cleavage surfaces are partly observed. As described above, the intergranular fracture that occurred in the uncharged specimen could be attributed to the segregated sulfur at the prior austenite grain boundaries (**Figure 1** (d)). Because the present 8Ni-0.1C as-quenched martensitic steel always exhibits intergranular fracture, it is an appropriate material to study the effect of hydrogen on this failure mechanism. Two-dimensional crack propagation morphologies are shown in the SEM images of **Figure 3** (d – f); (d) uncharged specimen, (e) hydrogen-charged specimen with H_D = 0.42 wt ppm, and (f) hydrogen-charged specimen with H_D = 4.00 wt ppm. The intergranular cracks propagated from the fatigue pre-cracks to the right in the images. The intergranular cracks in the uncharged specimen were notably meandering and branching (**Figure 3** (d)). In contrast, the morphology of the intergranular cracks in the hydrogen-charged specimens tended to be more continuous (**Figure 3** (e, f)).

Figure 4 presents the three-dimensional crack morphologies around the macroscopic crack tip reconstructed by X-ray CT using a × 4 optical magnifying lens in the (a, b) uncharged specimen (voxel size: 0.86^3 μm^3), (c, d) hydrogen-charged specimen with H_D = 0.42 wt ppm (voxel size: 1.52^3 μm^3), and (e, f) hydrogen-charged specimen with H_D = 4.00 wt ppm (voxel size: 0.87^3 μm^3). In **Figure 4** (b, d, f), the thickness of each crack component is expressed by the change in color according to the color bar inserted in the figures (min: 5.0 μm, max: 25.0 μm). The specimen coordinate system in the

present study is defined as ± *X*: the macroscopic tensile axis (parallel to the load-line displacement), - *Y*: the macroscopic crack propagation direction, and ± *Z*: the thickness direction of the compact tension specimen. The crack regions in the absorption images were segmented by machine learning with the U-net function using ORS Dragonfly Pro software. After meshing the segmented crack region, the thickness between the boundary points was calculated as the diameter of a hypothetical sphere fitting into each boundary point. In the uncharged specimen (**Figure 4** (a)), the three-dimensional crack morphology is not continuous and there are a lot of macroscopically isolated non-cracked regions (so called un-cracked ligaments). This indicates that the crack propagated discontinuously and that the crack was locally arrested. As reported previously, the discontinuous crack propagation could be attributed to the high crack arrestability of low-angle boundary segments [31]. In contrast, both the number and size of macroscopically un-cracked ligaments are small in the hydrogen-charged specimen (**Figure 4** (c, e)), indicating that the hydrogen-related intergranular cracks propagated more continuously.

Figure 5 (a – c) presents the crack thickness profiles in the volume of 600^3 μm^3 around the macroscopic crack tip; (a) uncharged specimen, (b) hydrogen-charged specimen with H_D = 0.42 wt ppm, and (c) hydrogen-charged specimen with H_D = 4.00 wt ppm. The average thickness of the hydrogen-charged specimens tends to be small (3.27 ± 0.48 μm (H_D = 0.42 wt ppm) and 3.76 ± 0.69 μm (H_D = 4.00 wt ppm)) compared to that of the uncharged specimen (4.45 ± 0.96 μm). The crack-tip opening angle (CTOA) estimated from the average crack thickness divided by the analyzed crack

length (600 μm) is 0.00741 (uncharged specimen), 0.0055 (hydrogen-charged specimen with H_D = 0.42 wt ppm), and 0.0062 (hydrogen-charged specimen with H_D = 4.00 wt ppm). The results indicate that the hydrogen-related intergranular crack propagated while maintaining a small crack opening-displacement. However, increasing H_D does not simply decrease the average crack thickness and CTOA. This could be due to the fact that the mechanical responses were scattered depending on the individual specimen as confirmed by the $J - \Delta a$ curves shown in **Figure 2** (a). **Figure 5** (d) presents the relationship between the crack thickness and exact *J*-integral value at the actual crack length of the specimens used for X-ray CT measurements. We can find a clear tendency for the *J*-integral value to increase monotonically with increasing crack thickness.

The energy criterion for fracture is that the strain energy release rate reaches the fracture energy (w_f) which includes the cack surface energy (γ_s) and plastic work (γ_p) [41-43]. Although the contribution of plastic work to fracture in metallic materials is considerably high even for brittle fracture [30], the results in the present study are insufficient to discuss the effect of plastic work on macroscopic mechanical properties. A clear reason for the degradation of mechanical properties by hydrogen-related intergranular fracture is the hydrogen-induced reduction of cohesive energy of prior austenite grain boundaries. In addition to those factors, we focus on the effect of crack morphology on mechanical responses and consider three parameters representing crack morphology that are related to crack surface energy: crack surface area (S), projected crack surface area on the YZ plane (S_p), and crack surface area at each YZ section (S_s). The analyzed length (parallel to Y direction) is ~ 1200 μm

from the crack tip. **Figure 6** (a) schematically explains these three parameters. Because the load-line displacement in the compact tension specimen is parallel to the ± *X* direction, the *YZ* plane corresponds to the macroscopic crack plane. For an ideal brittle material, the crack plane is uniform and only *S* needs to be estimated. On the other hand, when crack is meandering and branching as confirmed by the three-dimensional crack morphologies (**Figure 4**), the degrees of meandering and branching could affect the macroscopic fracture energy. According to Anderson's textbook [44], the fracture energy in materials with crack meandering and branching can be expressed as:

$$w_f = \gamma_s \frac{S}{S_p} \qquad \text{Eq.2}$$

The *J*-integral is defined as the potential energy per unit area released by crack propagation, and the *J*-integral increases as the estimated value of S / S_p increases, as shown in **Figure 6** (b).

As shown in **Figure 4**, the intergranular crack propagated discontinuously with the remaining un-cracked ligaments in the uncharged specimen, while the morphology of the intergranular crack was more continuous, and the uncracked ligaments tended to be smaller in the hydrogen-charged specimens. Because crack propagation with more meandering would consume more fracture energy, we can assume that the degree of crack meandering could affect the crack-growth resistance. **Figure 6** (c) shows the relative surface areas at each *YZ* section (i.e., surface area on a *YZ* section (S_s) divided by surface area (S)), and the vertical axis expresses the distance from the center section along *X* direction. The relative surface areas in the hydrogen-charged specimens are large around the center section, indicating that the degree of crack meandering is smaller in the hydrogen-charged specimens.

We can consider that the standard deviation of each curve in **Figure 6** (c) (i.e., 259 μm (uncharged specimen), 145 μm (hydrogen-charged specimen with H_D = 0.42 wt ppm), and 103 μm (hydrogen-charged specimen with H_D = 4.00 wt ppm) represents the degree of crack meandering and define it as "crack-propagated thickness". As shown in **Figure 6** (d), the crack-propagated thickness and tearing modulus have a clear correlation, i.e., larger crack-propagated thickness resulted in larger tearing modulus (crack-growth resistance). Accordingly, we can say that crack meandering also increases the crack-growth resistance.

The small meandering of the hydrogen-related crack propagation could be attributed to the fact that, even when the intergranular crack is locally arrested at a specific segment of prior austenite grain boundary (particularly, a low-angle boundary segment), the crack can continue to propagate into the grain interior as a quasi-cleavage manner in the hydrogen-charged specimens [32]. That is, the crack does not necessarily propagate along the prior austenite grain boundary, which is largely inclined from the macroscopic crack plane (*YZ* plane) (i.e., the boundary where the resolved normal stress is low), but can propagate along {011} plane, which is nearly parallel to the *YZ* plane with larger resolved normal stress, in a quasi-cleavage manner [45, 46].

As shown in **Figures 4 – 6**, the crack morphologies reflect the macroscopic mechanical responses (such as *J*-integral and tearing modulus). Obviously, the data obtained in the present study are limited. However, the results shown above suggest that systematic analyses in the future will allow the estimation of the mechanical response during operation from the resultant crack morphology.

4. Summary

The present study investigated hydrogen-related intergranular cracks in 8Ni-0.1C as-quenched martensitic steel. We proposed several parameters related to crack morphology: crack thickness, crack surface area, projected crack surface area on the *YZ* plane (macroscopic crack plane), and crack surface area at each *YZ* section, and investigated the relationship between macroscopic mechanical responses and crack morphology. The main results are as follows.

(1) The X-ray CT images showed that the three-dimensional crack morphology was not continuous, and there were a lot of un-cracked ligaments in the uncharged specimen. This indicates that the crack propagated discontinuously. In contrast, both the number and size of un-cracked ligaments were small in the hydrogen-charged specimen, indicating that the hydrogen-related intergranular cracks propagated more continuously. In addition, the hydrogen-related intergranular crack propagated while maintaining a smaller crack opening-displacement.

(2) We quantitatively evaluated the crack thickness and surface areas from the X-ray CT results and found the clear tendency that the *J*-integral value monotonically increased with increasing crack thickness. The *J*-integral also increased with increasing estimated values of the surface area divided by the projected surface area (S / S_p), indicating that the crack meandering and branching increased the fracture energy.

(3) From the value of the crack surface area at each *YZ* section (S_s) divided by the crack surface area

(S), we defined crack-propagated thickness (standard deviation of (S_s / S)) as a parameter representing crack meandering. The tearing modulus increased as the crack-propagated thickness increased, suggesting that crack meandering also increased the crack-growth resistance.

Acknowledgments

This work was financially supported by JST PRESTO (Grant Number JPMJPR2096), JSPS KAKENHI (Grant Numbers JP22K18910 and JP23H01717), and MEXT Program: Data Creation and Utilization Type Material Research and Development Project Grant Number JPMXP1122684766.

References

1) S. Lynch: *Corros. Rev.,* **30** (2012), 105-123.

https://doi.org/10.1515/corrrev-2012-0502

2) I.M. Robertson, P. Sofronis, A. Nagao, M.L. Martin, S. Wang, D.W. Gross and K.E. Nygren: *Metall. Mater. Trans. B*, **46** (2015), 1085-1103.

https://doi.org/10.1007/s11663-015-0325-y

3) A.S. Tetelman and W.D. Robertson: *Acta Metall*., **11** (1963), 415-426.

https://doi.org/10.1016/0001-6160(63)90166-4

4) R.A. Oriani and P.H. Josephic: *Acta Metall*., **22** (1974), 1065-1074.

https://doi.org/10.1016/0001-6160(74)90061-3

5) W.W. Gerberich and Y.Y. Chen: *Metall. Trans. A*, **65A** (1975), 271-278.

https://doi.org/10.1007/BF02667281

6) R.A. Oriani and P.H. Josephic: *Acta Metall*., **25** (1977), 979-988.

https://doi.org/10.1016/0001-6160(77)90126-2

7) C.D. Beachem: *Metall. Trans. A*, **3** (1972), 437-451.

https://doi.org/10.1007/BF02642048.

8) H.K. Birnbaum and P. Sofronis: *Mater. Sci. Eng. A*, **A176** (1994), 191-202.

https://doi.org/10.1016/0921-5093(94)90975-X

9) P.J. Ferreira, I.M. Robertson and H.K. Birnbaum: Acta Mater., **46** (1998), 1749-1757.

https://doi.org/10.1016/S1359-6454(97)00349-2

10) I.M. Robertson: *Eng. Fract. Mech*., **64** (1999), 649-673.

https://doi.org/10.1016/S0013-7944(99)00094-6

11) M. Nagumo: *ISIJ Int*., **41** (2001), 590-598.

https://doi.org/10.2355/isijinternational.41.590

12) M. Nagumo and H. Matsuda: *Phil. Mag. A*, **82** (2002), 3415-3425.

https://doi.org/10.1080/01418610208240452

13) Y. Hagihara, T. Shobu, N. Hisamori, H. Suzuki, K. Takai and K. Hirai: *ISIJ Int*., **52** (2012), 298-306.

https://doi.org/10.2355/isijinternational.52.298

14) A.R. Marder and G. Krauss: *Trans. ASM*, **60** (1967), 651-660.

15) S. Morito, H. Tanaka, R. Konishi, T. Furuhara and T. Maki: *Acta Mater*., **51** (2003), 1789-1799.

https://doi.org/10.1016/s1359-6454(02)00577-3

16) S. Morito, X. Huang, T. Furuhara, T. Maki and N. Hansen: *Acta Mater*., **54** (2006), 5323-5331.

https://doi.org/10.1016/j.actamat.2006.07.009

17) A. Shibata, G. Miyamoto, S. Morito, A. Nakamura, T. Moronaga, H. Kitano, I. Gutierrez-Urrutia, T. Hara and K. Tsuzaki: *Acta Mater*., **246** (2023), 118675.

https://doi.org/10.1016/j.actamat.2023.118675

18) A. Shibata, H. Takahashi and N. Tsuji: *ISIJ Int*., **52** (2012), 208-212.

https://doi.org/10.2355/isijinternational.52.208

19) A. Shibata, T. Murata, H. Takahashi, T. Matsuoka and N. Tsuji: *Metall. Mater. Trans. A*, **46** (2015), 5685-5696.

https://doi.org/10.1007/s11661-015-3176-x

20) A. Shibata, Y. Momotani, T. Murata, T. Matsuoka, M. Tsuboi and N. Tsuji: *Mater. Sci. & Technol*., **33** (2017), 1524-1532.

https://doi.org/10.1080/02670836.2017.1312210

21) A. Shibata, T. Yonemura, Y. Momotani, M.-H. Park, S. Takagi, Y. Madi, J. Besson and N. Tsuji: *Acta Mater*., **210** (2021), 116828.

https://doi.org/10.1016/j.actamat.2021.116828

22) S.K. Banerji, C.J. McMahon Jr and H.C. Feng: *Metall. Mater. Trans. A*, **9A** (1978), 237-247.

https://doi.org/10.1007/BF0264670

23) B. Craig and G. Krauss: *Metall. Mater. Trans. A*, **11A** (1980), 1799-1808.

https://doi.org/10.1007/BF02655095

24) S.J. Lee, J.A. Ronevich, G. Krauss and D.K. Matlock: *ISIJ Int*., **50** (2010), 294-301.

https://doi.org/10.2355/isijinternational.50.294

25) Y. Momotani, A. Shibata, D. Terada and N. Tsuji: *Int. J. Hydro. Energy*, **42** (2017), 3371-3379.

https://doi.org/10.1016/j.ijhydene.2016.09.188

26) M. Yamaguchi, K.-I. Ebihara, M. Itakura, T. Kadoyoshi, T. Suzudo and H. Kaburaki: *Metall.*

Mater. Trans. A, **42** (2010), 330-339.

https://doi.org/10.1007/s11661-010-0380-6

27) M. Yamaguchi, J. Kameda, K.-I. Ebihara, M. Itakura and H. Kaburaki: *Phil. Mag*., **92** (2012), 1349-1368.

https://doi.org/10.1080/14786435.2011.645077

28) K.N. Solanki, M.A. Tschopp, M.A. Bhatia and N.R. Rhodes: *Metall. Mater. Trans. A*, **44A** (2013), 1365-1375.

https://doi.org/10.1007/s11661-012-1430-z

29) M. Yamaguchi, K.-I. Ebihara and M. Itakura: *Corros. Rev*., **33** (2015), 547-557.

https://doi.org/10.1515/corrrev-2015-0039

30) M. Yamaguchi and J. Kameda: *Phil. Mag*., **94** (2014), 2131-2149.

https://doi.org/10.1080/14786435.2014.906757

31) A. Shibata, I. Gutierrez-Urrutia, A. Nakamura, G. Miyamoto, Y. Madi, J. Besson, T. Hara and K. Tsuzaki: *Acta Mater*., **234** (2022), 118053.

https://doi.org/10.1016/j.actamat.2022.118053

32) A. Shibata, I. Gutierrez-Urrutia, A. Nakamura, K. Okada, G. Miyamoto, Y. Madi, J. Besson, T. Hara and K. Tsuzaki: *Int. J. Hydro. Energy*, **48** (2023), 34565-34574.

https://doi.org/10.1016/j.ijhydene.2023.05.211

33) A.R. Rosenfield and B.S. Majumdar: *Nucl. Eng. Des*., **105** (1987), 51-57.

https://doi.org/10.1016/0029-5493(87)90228-7

34) M.Y. He, D.J. Wissuchek and A.G. Evans: *Acta Mater*., **45** (1997), 2813-2820.

https://doi.org/10.1016/S1359-6454(96)00385-0

35) F. Yanagimoto, T. Hemmi, Y. Suzuki, Y. Takashima, T. Kawabata and K. Shibanuma: *Acta Mater*., **177** (2019), 96-106.

https://doi.org/10.1016/j.actamat.2019.06.038

36) Y. Takashima, T. Kawabata, R. Deguchi, S. Yamada and F. Minami: *Theor. Appl. Fract. Mech*., **101** (2019), 365-372.

https://doi.org/10.1016/j.tafmec.2019.02.013

37) T. Kawabata, F. Tonsho, Y. Nishizono, N. Nakamura and Y. Takashima: *Theor. Appl. Fract. Mech*., **100** (2019), 171-180.

https://doi.org/10.1016/j.tafmec.2019.01.010

38) A. Shibata, Y. Madi, K. Okada, N. Tsuji and J. Besson: *Int. J. Hydro. Energy*, **44** (2019), 29034-29046.

https://doi.org/10.1016/j.ijhydene.2019.09.097

39) ASTM E1820-17 Standard Test Method for Measurement of Fracture Toughness, 2017.

40) D. Bika, J.A. Pfaendtner, M. Menyhard and C.J. McMahon Jr: *Acta Metall. Mater.*, **43** (1995), 1895-1908.

https://doi.org/10.1016/0956-7151(94)00388-X

41) A. Griffith: *Phil. Trans. R. Soc. of Lond. A*, **221** (1921), 163-198.

https://doi.org/10.1098/rsta.1921.0006

42) E. Orowan: *Rep. Prog. Phys*., **12** (1949), 185-232.

https://doi.org/0.1088/0034-4885/12/1/309

43) G.R. Irwin: *J. Appl. Mech*., **24** (1957), 361-364.

https://doi.org/10.1115/1.4011547

44) T.L. Anderson: Fracture Mechanics, Fourth edition, CRC Press, New York, (2017), 35.

45) K. Okada, A. Shibata, H. Matsumiya and N. Tsuji: *ISIJ Int*., **62** (2022), 2081-2088.

https://doi.org/10.2355/isijinternational.ISIJINT-2022-212

46) K. Okada, A. Shibata and N. Tsuji: *Scr. Mater*., **234** (2023), 115568.

https://doi.org/10.1016/j.scriptamat.2023.115568

Figure captions

Figure 1 (a) SEM image, (b, c) STEM images, and (d) STEM-EDX sulfur distribution map of the heat-treated specimen. The observation areas of (c) and (d) are identical.

Figure 2 (a) $J - \Delta a$ resistance curves of the uncharged specimen and hydrogen-charged specimens (H_D = 0.42 wt ppm and 4.00 wt ppm) and (b) change in tearing modulus with H_D (the data from previous study was reused [31, 38] (reproduced with permission from Elsevier)). The specimens used for the X-ray CT measurements are indicated by the arrows in (a).

Figure 3 SEM images of the (a – c) fracture surfaces and (d – f) two-dimensional crack morphologies of the (a, d) uncharged specimen, (b, e) hydrogen-charged specimen with H_D = 0.42 wt ppm, and (c, f) hydrogen-charged specimen with H_D = 4.00 wt ppm.

Figure 4 Three-dimensional crack morphologies reconstructed by X-ray CT of the (a, b) uncharged specimen, (c, d) hydrogen-charged specimen with H_D = 0.42 wt ppm, and (e, f) hydrogen-charged specimen with H_D = 4.00 wt ppm. The color in (b, d, f) expresses the thickness value of the crack components according to the color bar (Min: 5.0 μm, Max: 25.0 μm).

Figure 5 Crack thickness profiles in the (a) uncharged specimen, (b) hydrogen-charged specimen

with H_D = 0.42 wt ppm, and (c) hydrogen-charged specimen with H_D = 4.00 wt ppm. (d) The relationship between *J*-integral and crack thickness.

Figure 6 (a) Schematic illustration of crack surface area (*S*), projected crack surface area on the *YZ* plane (S_p), and crack surface area at each *YZ* section (S_s), (b) change in *J*-integral value as a function of S / S_p, (c) relative surface area on an each *YZ* section (S_s / S), (d) change in tearing modulus as a function of crack-propagated thickness.

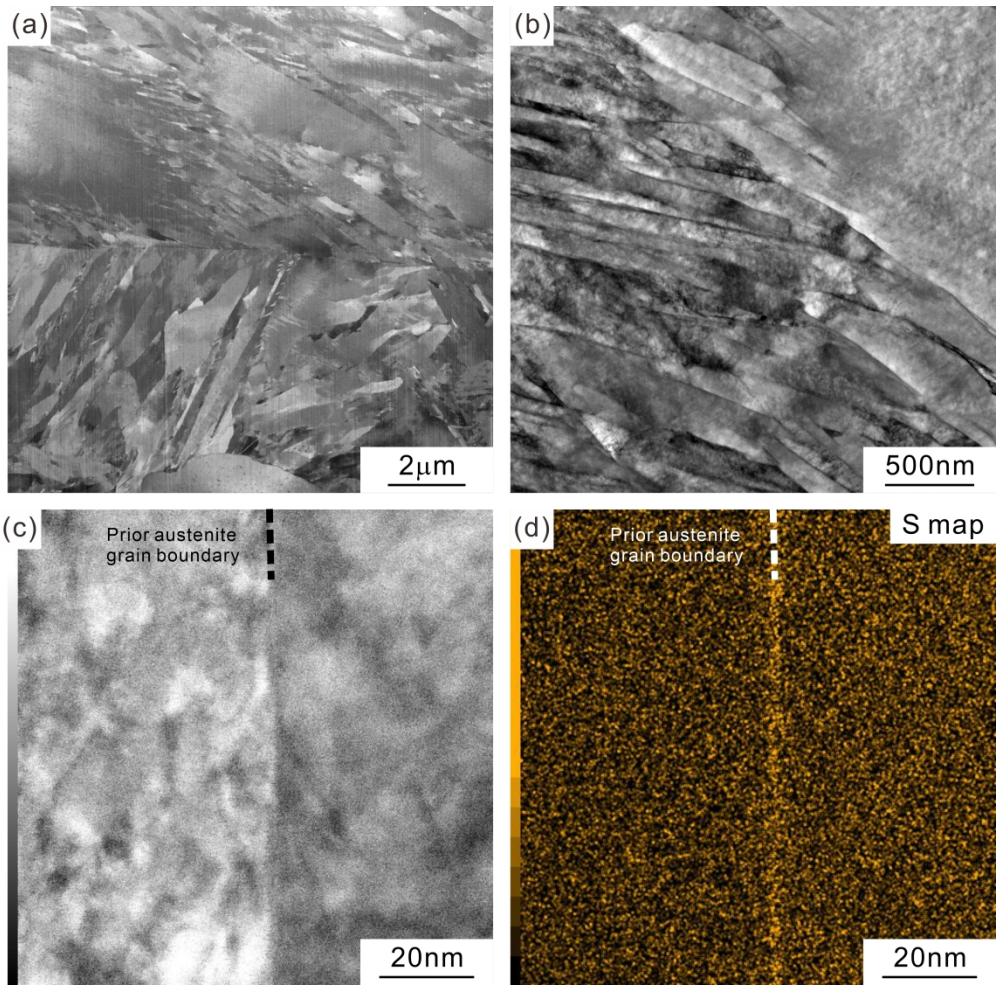

Figure 1 (a) SEM image, (b, c) STEM images, and (d) STEM-EDX sulfur distribution map of the heat-treated specimen. The observation areas of (c) and (d) are identical.

154x150mm (600 x 600 DPI)

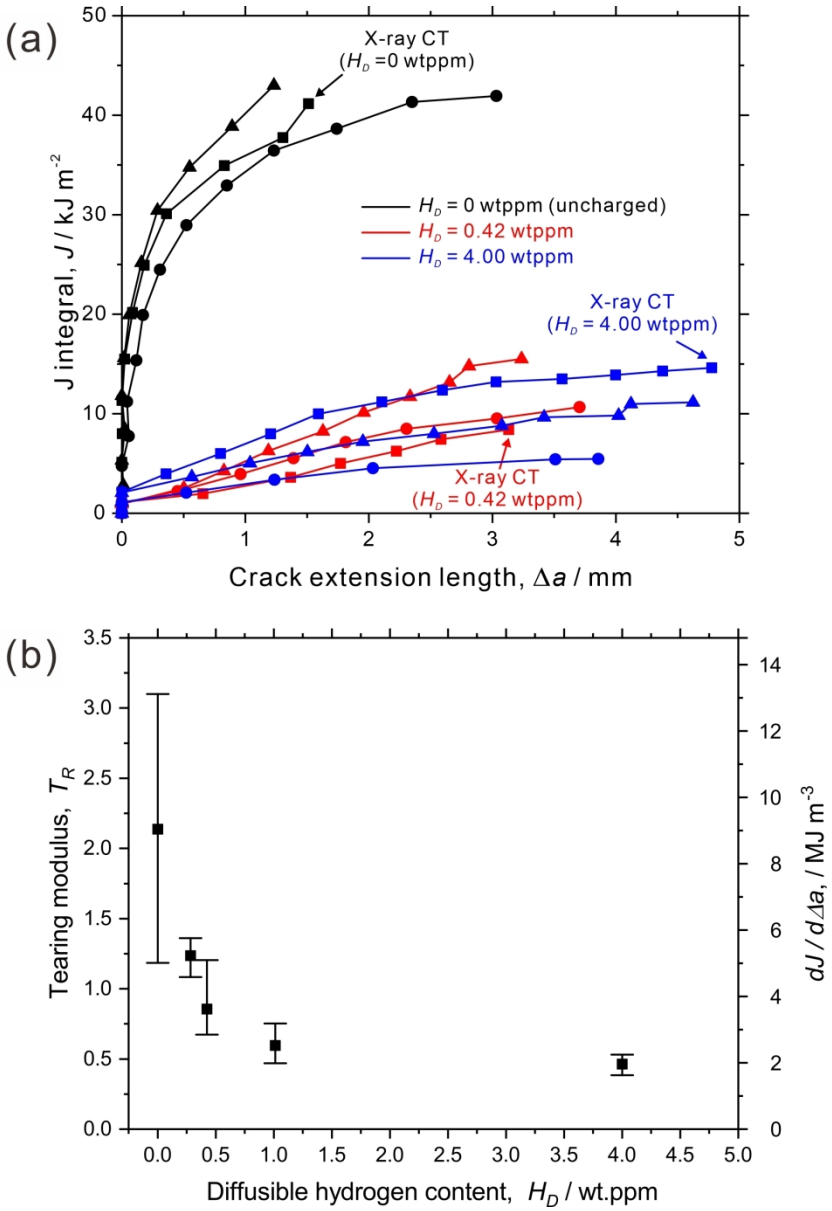

Figure 2 (a) $J - \Delta a$ resistance curves of the uncharged specimen and hydrogen-charged specimens (H_D = 0.42 wt ppm and 4.00 wt ppm) and (b) change in tearing modulus with H_D (the data from previous study was reused [31, 38]) (reproduced with permission from Elsevier)). The specimens used for the X-ray CT measurements are indicated by the arrows in (a).

88x128mm (600 x 600 DPI)

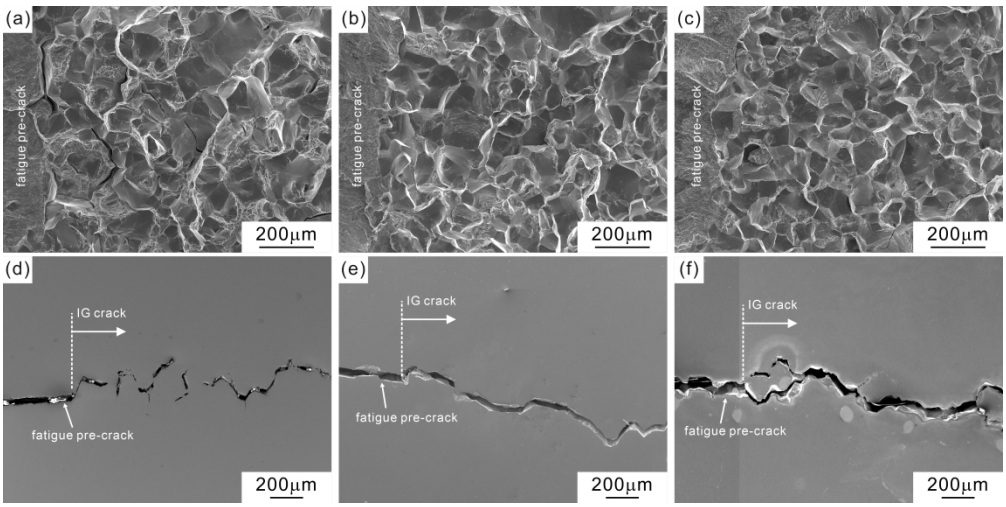

Figure 3 SEM images of the (a – c) fracture surfaces and (d – f) two-dimensional crack morphologies of the (a, d) uncharged specimen, (b, e) hydrogen-charged specimen with H_D = 0.42 wt ppm, and (c, f) hydrogen-charged specimen with H_D = 4.00 wt ppm.

228x113mm (600 x 600 DPI)

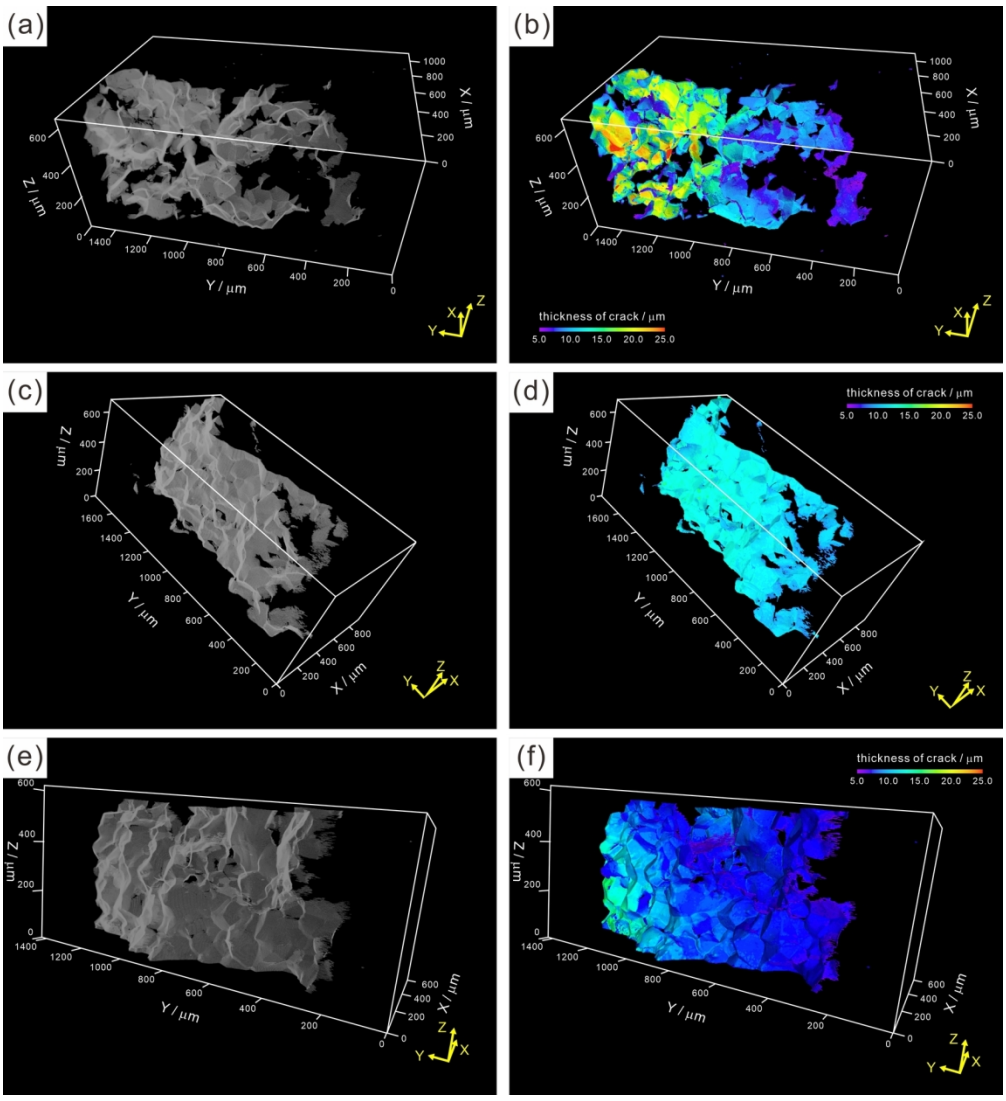

Figure 4 Three-dimensional crack morphologies reconstructed by X-ray CT of the (a, b) uncharged specimen, (c, d) hydrogen-charged specimen with H_D = 0.42 wt ppm, and (e, f) hydrogen-charged specimen with H_D = 4.00 wt ppm. The color in (b, d, f) expresses the thickness value of the crack components according to the color bar (Min: 5.0 μm, Max: 25.0 μm).

151x165mm (300 x 300 DPI)

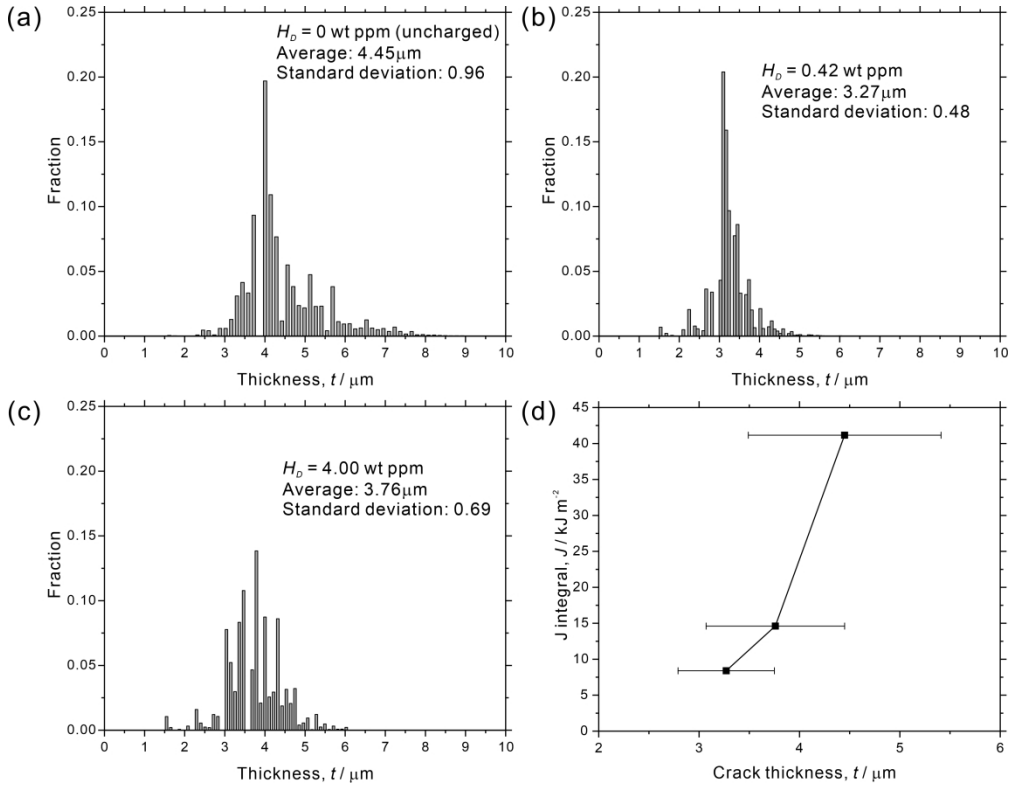

Figure 5 Crack thickness profiles in the (a) uncharged specimen, (b) hydrogen-charged specimen with H_D = 0.42 wt ppm, and (c) hydrogen-charged specimen with H_D = 4.00 wt ppm. (d) The relationship between J-integral and crack thickness.

161x124mm (600 x 600 DPI)

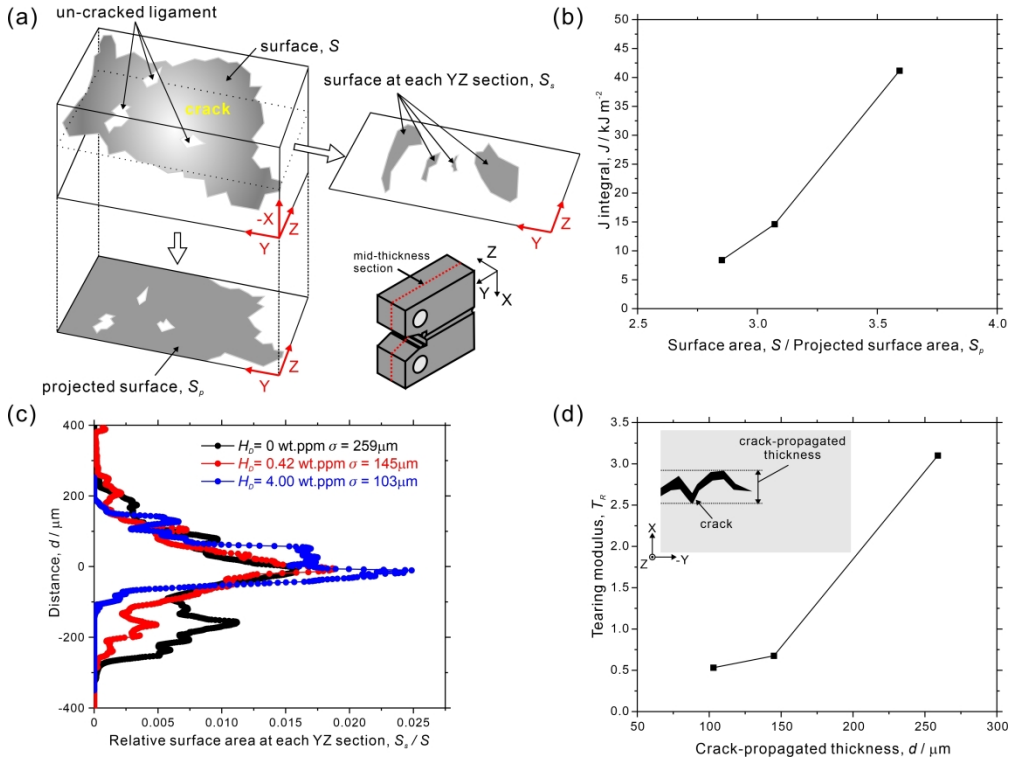

Figure 6 (a) Schematic illustration of crack surface area (*S*), projected crack surface area on the *YZ* plane (S_p), and crack surface area at each *YZ* section (S_s), (b) change in *J*-integral value as a function of S / S_p, (c) relative surface area on an each *YZ* section (S_s / S), (d) change in tearing modulus as a function of crack-propagated thickness.

182x137mm (600 x 600 DPI)

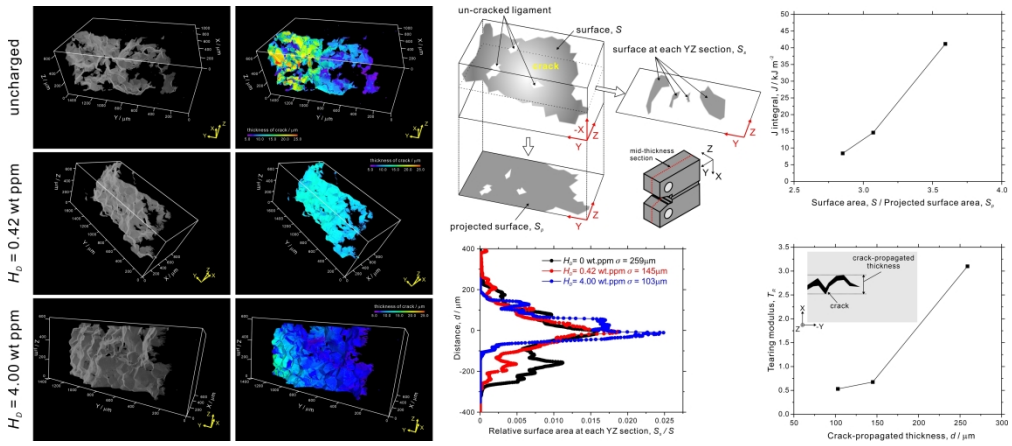

Graphical abstract

380x165mm (300 x 300 DPI)